# A Deep Learning Framework for Two-Dimensional, Multi-Frequency Propagation Factor Estimation

**Sarah E. Wessinger, Andrew J. Kammerer, Jacob Gull**
Naval Research Laboratory, Monterey, CA
Devine Consulting, Fremont, CA

**Leslie N. Smith**
US Naval Research Laboratory, Washington, DC

**Jonathan Gehman, Zachary Beever**
JHU Applied Physics Laboratory, Laurel, MD

## Abstract

Accurately estimating the refractive environment over multiple frequencies within the marine atmospheric boundary layer is crucial for the effective deployment of radar technologies. Traditional parabolic equation simulations, while effective, can be computationally expensive and time-intensive, limiting their practical application. This communication explores a novel approach using deep neural networks to estimate the pattern propagation factor, a critical parameter for characterizing environmental impacts on signal propagation. Image-to-image translation generators designed to ingest modified refractivity data and generate predictions of pattern propagation factors over the same domain were developed. Findings demonstrate that deep neural networks can be trained to analyze multiple frequencies and reasonably predict the pattern propagation factor, offering an alternative to traditional methods.

## Introduction

### Refractive Environment

The performance of radio frequency (RF) technologies is highly susceptible to environmental factors that influence signal propagation. Fluctuations in atmospheric conditions, particularly humidity, can significantly impact signal range and quality. This variability poses challenges across diverse applications, including communication and radar technologies which are critical to national defense as well as everyday RF devices like cell phones and data-relay networks. Therefore, understanding and mitigating these environmental effects is crucial for optimizing the reliability and performance of RF systems.

The power at the end of an RF path is given by the one-way radio transmission equation (Friis 1946; Freehafer et al. 1951):

$$P_r = P_t G_t G_r \left( \frac{F}{2k_0 R} \right)^2 \qquad (1)$$

where $P_r$ is power at a distance (slant range) $R$, $P_t$ is transmitted power, $G_t$ is the transmitter peak power gain, $G_r$ is the receiver peak power gain, $k_0$ is the RF wavenumber, and

$F$ is the one-way pattern propagation factor. The only variable in Equation 1 not determined by the radar system setup is $F$ as it encapsulates all environmental impacts on signal propagation. More specifically, $F$ is a measure of gain due to the environment. For practical applications, $F$ can also be expressed in decibels ($F_{dB}$). It is sometimes convenient to work with attenuation instead of gain using propagation loss in decibels ($P_L$):

$$P_L = 20 \log (2k_0 R) - 20 \log |F| \qquad (2)$$

$$F_{\text{dB}} = 10 \log |F| \qquad (3)$$

Accurately estimating $F$ (or, equivalently, $P_L$) is imperative for quantifying environmental attenuation on RF signals. Current methods rely on parabolic equation simulations, such as the advanced propagation model (APM; (Barrios 1994)), the variable terrain radio parabolic equation (VTRPE; (Ryan 1991)), and the tropospheric electromagnetic parabolic equation routine (TEMPER; (Rouseff 1992)). These simulations require inputs of modified refractivity ($M$) which is calculated from atmospheric refractivity using temperature in Kelvin ($T$), partial vapor pressure in millibar ($e$), and pressure in millibar ($p$) and adjusted to account for Earth's curvature (Bean and Dutton 1968):

$$M(z) = \left( \frac{77.6\,p}{T} + \frac{373,256\,e}{T^2} \right) + \frac{z}{R_e} \times 10^6 \qquad (4)$$

where $z$ is altitude and $R_e$ is Earth's radius. This study explores using deep neural networks (DNNs) to predict $F$ based on $M$. DNNs excel at approximating complex nonlinear relationships by performing regressions on extensive datasets. While computationally intensive to train, once trained, DNNs offer significant advantages in terms of speed and efficiency.

DNNs and other deep learning techniques have been previously applied to RF technologies, particularly for communication applications (Zhang et al. 2019; Gündüz et al. 2019; Yang et al. 2019; Bal et al. 2022). Notably, Bal et al. (2022) demonstrated the potential of DNNs in estimating the path loss exponent for wireless communication. However, to the authors' knowledge, no prior studies have applied DNNs to estimate $F$, $P_L$, or $F_{dB}$ over the entire domain of range and altitude.

DNNs have been used within radar applications for both forward and inverse problems (Wang, Tang, and Liao 2019;

Zhu et al. 2018; Pastore et al. 2022; Liao et al. 2023; Shu et al. 2023). Forward problems estimate the refractive environment using environmental data, while inverse problems estimate environmental conditions or perform object detection using the refractive environment. Estimating evaporation duct height (EDH) is a popular multivariate forward problem within the refractive environment, with prior studies employing DNNs (Zhu et al. 2018; Liao et al. 2023; Shu et al. 2023). Evaporation ducts, caused by steep near-surface vertical humidity gradients, are of interest because they trap RF waves and extend signal ranges at altitudes below the EDH. Because the layer of air where evaporation ducts form, within $\sim 30$ m of the ocean surface, is often turbulent there is a high degree of self-similarity among evaporation ducts within $M(z)$ profiles. This makes the estimation of EDH a generally easier problem for DNNs than learning RF signal propagation behavior based on any $M(z)$. This study focuses on a forward problem where numerical weather prediction data is used to estimate the refractive environment through $F$ or $P_L$.

Characterizing RF signal propagation is especially challenging in the marine atmospheric boundary layer due to constantly fluctuating thermodynamic variables. RF technologies operating in this environment commonly use S- and X-band frequencies, thus, accurately estimating the refractive environment across both bands is essential. Prior studies using DNNs for multi- frequency RF problems commonly train separate models for each frequency (Shu et al. 2023; Popoola et al. 2019). In contrast, this study trains a single DNN on a dataset comprised of two frequencies and then compares the two-frequency predictions to the individual frequency predictions. Additionally, prior research has primarily focused on attenuation as a function of only range or altitude but not both simultaneously (Shu et al. 2023; Nguyen and Cheema 2021; Moraitis et al. 2021; Xu et al. 2021). To the authors' knowledge, estimating $F$ simultaneously over both range and altitude using DNNs has not yet been attempted.

This study makes three novel contributions: (1) It demonstrates the capability of a trained DNN to accurately estimate the pattern propagation factor, (2) it achieves this estimation over both altitude and range, and (3) it introduces a unified DNN framework capable of accounting for multiple frequencies.

### Image-to-Image Translation

Image-to-image translation is a powerful machine learning technique that enables the transformation of an image from one domain, characterized by a specific set of attributes, to another domain with new attributes, while preserving the essential content of the original image (Isola et al. 2017; Zhu et al. 2017). This process involves learning the intricate mapping between the two domains, allowing for a wide range of applications in image processing, including image generation, style transfer, and segmentation (Pang et al. 2021). In this context, the $M$ domain (i.e., modified refractivity) is the input "image" and the $F$ domain is the desired output "image".

In recent years, deep learning frameworks have rev-

olutionized the field of image-to-image translation, with autoencoders, convolutional neural networks (CNNs), and generative adversarial networks (GANs) achieving remarkable success. GANs, in particular, have emerged as a popular choice for image-to-image translation tasks, due to their ability to learn complex mappings between domains. A typical GAN architecture for image-to-image translation consists of two primary components: a generator network and a discriminator network. The generator network produces an image in the output domain, while the discriminator network evaluates the generated images, providing feedback to the generator to improve its performance.

### Neural Network-Based Emulator Architecture

Initially, GAN architecture was implemented for image-to-image translation, as it is a widely accepted architecture for this task. The discriminator in a GAN plays a crucial role in guiding the generator by assessing the realism of the generated images. Through adversarial training, the discriminator enforces realism by distinguishing fine details, textures, and patterns that align with the desired target distribution. This feedback loop enables the generator to iteratively refine its outputs, ensuring they match the statistical properties of the real data. However, in this study, supervised training with explicitly desired outputs renders the adversarial training unnecessary and only the generator was needed.

U-Net architectures (Ronneberger, Fischer, and Brox 2015) are commonly employed as the generator in GANs (Ronneberger, Fischer, and Brox 2015). Their architecture is characterized by a contracting and an expanding block, connected by skip connections and an inner module. Skip connections enable the model to detect features at multiple resolutions, capturing both global structural relationships and pixel-wise details. This design allows the U-Net to effectively learn the complex mappings between domains, making it an ideal choice for image-to-image translation tasks.

This study evaluated the merits of implementing a variety of UNet-based generator architectures. The following lists the models tested in order of size and complexity:

- Two versions of U-Net (Ronneberger, Fischer, and Brox 2015)
- Recursive Neural Network (RNN)
- Efficient U-Net (Tan and Le 2019)
- Dilated U-Net (Wang et al. 2020)
- UVCGan v1 and v2 (Visual Transformer at bottleneck) (Torbunov et al. 2023b; 2023a)
- UCTransNet (transformer instead of skip connections) (Wang et al. 2022)
- A novel hybrid (combines UVCGan and UCTransNet)

We observed significant improvements in performance from the first U-Nets test to the larger and more complex models. However, our evaluations demonstrated that architectural innovations alone were approaching the limits of significant performance gains. While initial gains underscore the importance of exploring alternative architectures, the final two models only provided minor performance improvements but

with an increase in computational cost. Consequently, UVC-GANv2 is the default model used in this study. The UVC-GANv2 architecture, henceforth referred to as "RefractNet", is illustrated in Figure 1.

## Methods

### Data

$M(z)$ used within this study are from the Naval Research Laboratory's numerical weather prediction system, the Coupled Ocean Atmosphere Mesoscale Prediction System (COAMPS®). COAMPS® forecasts were run for 7 arbitrary oceanic locations across the globe to remove local geographic dependence on these results.

The physics-based parabolic simulation used to calculate the refractive domain of $F$ from the $M(z)$ is TEMPER version 3.2.3. TEMPER was run for two frequencies, 3 and 10 GHz (S- and X-Band, respectively), assuming a smooth sea surface. Rough ocean surfaces could be an added complexity at a later time; the point of this study was just an initial proof-of-concept focusing on refractivity, $M(z)$. The antenna height was set to 20 m for each simulation. 70,322 cases comprised of an $M$ input and a refractive domain output were used to train RefractNet and 15,070 cases were used to test it. Half of the cases for both the test and train datasets are X-Band, and half are S-Band. We expect this number of training samples to be sufficient to train our network because several well-known image benchmark datasets contain on the order of 50,000 training samples (i.e., MNIST, Cifar-10/100). Note, $M$ is assumed homogeneous over range and time for this study (Figure 2). TEMPER simulations for S- and X-band have varying domain altitudes based on mean sea level. All S-Band runs range in altitude from MSL (0m) to 300m, whereas X-band runs extend from the MSL (0m) to 30m, both at a 0.2 m resolution.

### Metrics

In addition to visual inspection of individual examples, this study leveraged a combination of three key performance metrics: Mean Squared Error (MSE), Structural Similarity (SSIM), and Fréchet Inception Distance (FID). Mean Squared Error (MSE) is a widely used metric that calculates the average squared difference between the pixel values of real and generated images, penalizing larger errors more heavily. However, as a pixel-wise measure, MSE is limited in capturing larger-scale structural trends, which are critical in evaluating the accuracy of complex images. In contrast, Structural Similarity (SSIM) (Wang et al. 2004) assesses error while considering structural information and broader trends, yielding a score between 0 (no similarity) and 1 (perfect similarity). Utilizing convolutional properties, SSIM effectively identifies low-level structures within images, which is critical for evaluating the accuracy of the main structure. Fréchet Inception Distance (FID) (Yu, Zhang, and Deng 2021) is the most common metric used to evaluate GAN results as it compares features extracted from real and generated images using a pre-trained network, with lower scores indicating better fidelity to real images. SSIM and FID are particularly useful in evaluating the performance of

Table 1: Combinations of variables used to train the RefractNet for each experiment

| Experiment Number | Variable, Altitude, Frequencies |
|---|---|
| Experiment 1 | $F$, 30 m, X + S |
| Experiment 2 | $F$, 30 m, X |
| Experiment 3 | $F$, 30 m, S |
| Experiment 4 | $F_{dB}$, 30 m, X + S |
| Experiment 5 | $F_{dB}$, 30 m, X |
| Experiment 6 | $F_{dB}$, 30 m, S |
| Experiment 7 | $F$, 300 m, S |
| Experiment 8 | $F_{dB}$, 300 m, S |

the emulator as they provide a more comprehensive and nuanced understanding of the output quality.

Each metric can be computed for individual samples, batches, frequency, and depth categories, enabling clustering analyses to identify classes of inputs where the model performs poorly. This is particularly useful in identifying areas where the model requires improvement and guides the approach used to optimize the emulator's performance. As such, during RefractNet's development, these metrics guided efforts to improve the model's accuracy through various methods, including data augmentation, loss function optimization, hyper-parameter tuning, and experimentation with different U-Net architectures.

## Experiments

### Setup

Eight experiments were conducted during this study (Table 1). Input/output domains having 256 x 256 pixels is optimal for a balance between performance and speed. To meet this requirement, $M(z)$ is interpolated to have 256 equally spaced points over the evaluated altitudes (i.e., 0-30m or 0-300m) and repeated 256 times over range (Figure 2). The corresponding domains of $F$ were interpolated to have the same points over altitude and range as the $M$ domains (256 x 256). Input and output domains were scaled to have values between 0 and 1 due to batch normalization layers within the architecture. As such all data points for $M$ domain images and $F$ domain images are normalized based on altitude and gain variable following the normalization schemes in Table 2.

In addition, single frequency experiments have half the number of training samples as the dual frequency experiments as previously described. Thus, RefractNet was trained twice as long (i.e., double the number of epochs) for single-frequency experiments in order to minimize any training advantage the dual-frequency experiments might gain by having twice as many training samples.

### Results

Each evaluation metric (MSE, FID, SSIM) is calculated between the RefractNet-predicted refractive domain image
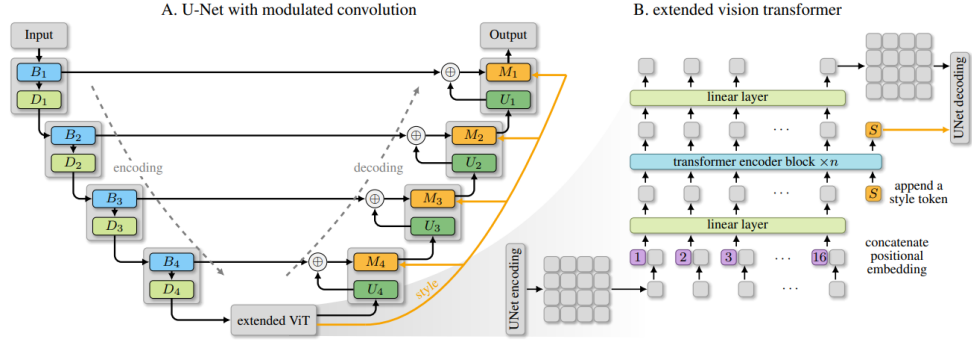
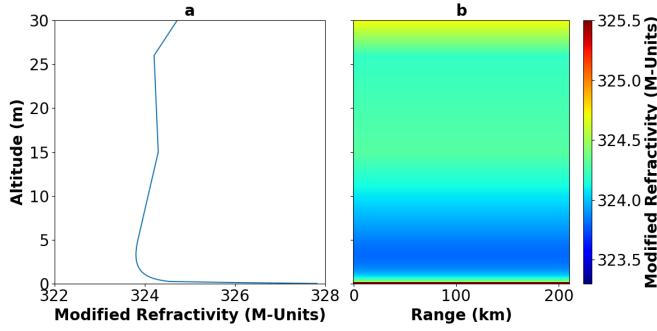Figure 1: UVCGANv2, "RefractNet", Generator Architecture.



Figure 2: (a) $M(z)$ used to create the (b) range-homogeneous $M$ domain input for RefractNet.

Table 2: Normalization Schemes Used Based on Altitude and Gain Variable

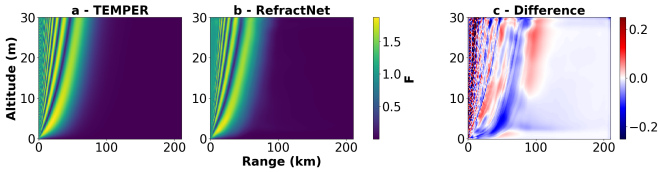| Altitude, Variable | $M(z)$ Norm. | Refractive Norm. |
|---|---|---|
| 30 m, $F$ | $M = \frac{M-288}{181}$ | $F = \frac{F}{16.45}$ |
| 300 m, $F$ | $M = \frac{M-282}{187}$ | $F = \frac{F}{16.45}$ |
| 30 m, $F_{dB}$ | $M = \frac{M-288}{181}$ | $F_{dB} = \frac{F_{dB}+90.01}{-102.17}$ |
| 300 m, $F_{dB}$ | $M = \frac{M-282}{187}$ | $F_{dB} = \frac{F_{dB}+90.01}{-102.17}$ |



Figure 3: Refractive domain of $F$ calculated by (a) TEMPER, (b) RefractNet, and (c) the difference between these domains, TEMPER-RefractNet, from a case in Experiment 1 where the evaluation metrics are: MSE = $1.15 \times 10^{-5}$, FID = 0.002, and SSIM = 0.89.
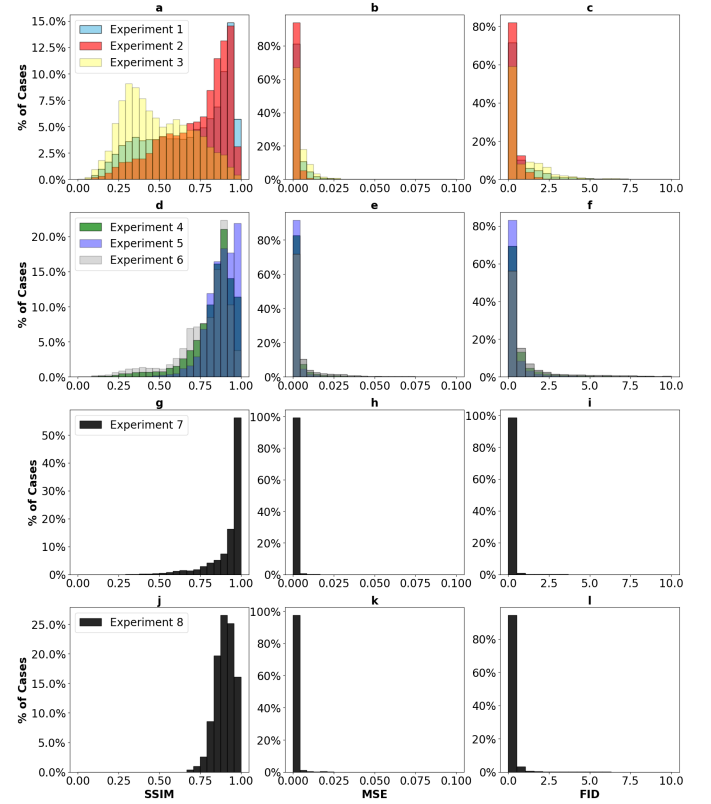


Figure 4: Distribution of evaluation metrics for SSIM (a, d, g, j), MSE (b, e, h, k), and FID (c, f, i, l) for Experiments 1-3 (a-c), 4-6 (d-f), 7 (g-i), and 8 (j-l).

and TEMPER's normalized calculated refractive domain image for each test case in each experiment (Figure 3), thus these values are dimensionless and comparable. Distribu- tions of evaluation metrics, presented in Figure 4, demon- strate that RefractNet performs well across a variety of sce- narios. The majority of cases exhibit high SSIM values (in- dicating strong structural similarity between predictions and TEMPER) and low FID and MSE values (demonstrating low dissimilarity and error). Figure 5 illustrates a case that per- formed poorly due to having ducting (trapping) features at longer ranges, which are indicative of signal interference due to environmental reflection and/or refraction.
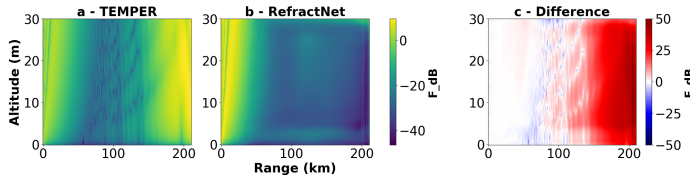
Figure 5: Refractive domain of $F_{dB}$ calculated by (a) TEMPER, (b) RefractNet, and (c) the difference, TEMPER-RefractNet, between these domains for a case from Experiment 6 where the evaluation metrics are: MSE = 0.03, FID = 6.88, and SSIM = 0.65.

Table 3: Average values of evaluation metrics for each experiment.

| Experiment Number | MSE | FID | SSIM |
|---|---|---|---|
| Experiment 1 | 0.002 | 0.55 | 0.68 |
| Experiment 2 | 0.001 | 0.23 | 0.73 |
| Experiment 3 | 0.003 | 0.88 | 0.49 |
| Experiment 4 | 0.004 | 1.01 | 0.83 |
| Experiment 5 | 0.002 | 0.42 | 0.88 |
| Experiment 6 | 0.007 | 1.67 | 0.78 |
| Experiment 7 | 0.000 | 0.06 | 0.92 |
| Experiment 8 | 0.001 | 0.21 | 0.90 |

To rigorously assess RefractNet's capacity to handle multiple frequencies, the performance of single-frequency experiments against their dual-frequency counterparts was statistically compared. Specifically, two-sample t-tests were performed on the MSE, SSIM, and FID populations for the following experiment pairs, ensuring consistent altitude and gain variables: Experiments 1 & 2, Experiments 1 & 3, Experiments 4 & 5, and Experiments 4 & 6. The P-values from each two sample t-tests were <0.05, indicating all null hypotheses (e.g., Average MSE Experiment 1 = Average MSE Experiment 3) are rejected, and the average values, as detailed in Table 3, of these evaluation metrics are different in a statistically significant sense.

Interestingly, X-band only experiments (Exp. 2 & 5) consistently outperformed both S-band-only (Exp. 3 & 6) and dual-frequency experiments (Exp. 1 & 4) across all metrics (Table 3). This highlights an important consideration: RF signal propagation becomes increasingly sensitive to atmospheric refractive structures at higher frequencies (Lentini and Hackett 2015). Consequently, the refractive domain exhibits more distinct and repetitive patterns at higher frequencies, potentially contributing to more robust and effective DNN training.

Despite evaluation metrics performing better for X-band-only training, dual-frequency-trained experiments yield similar patterns within the refractive domains (Figure 6), and similar average evaluation metric values for each individual frequency in dual-frequency experiments (Table 4) compared to single-frequency-trained experiments. Thus, this

Table 4: Average values of evaluation metrics for each frequency in dual frequency experiments.

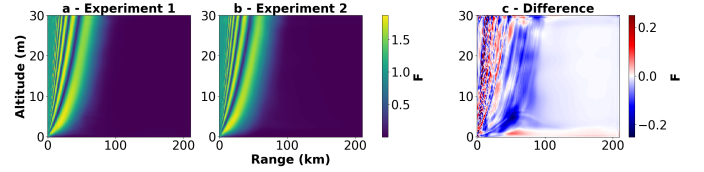| Experiment Number, Frequency | MSE | FID | SSIM |
|---|---|---|---|
| Experiment 1, X | 0.001 | 0.23 | 0.75 |
| Experiment 1, S | 0.003 | 0.87 | 0.60 |
| Experiment 4, X | 0.002 | 0.41 | 0.87 |
| Experiment 4, S | 0.006 | 1.60 | 0.78 |



Figure 6: Refractive domain of $F$ for the same case in both (a) Experiment 1 with metrics of MSE = 1.15x10$^{-5}$, FID = 0.002, and SSIM = 0.89, and (b) Experiment 2 of MSE = 8.64x10$^{-6}$, FID = 0.001, and SSIM = 0.92 and (c) the difference between these domains.

DNN framework is able to account for two frequencies.

To further investigate RefractNet's performance, predictions of $F$ versus $F_{dB}$ domains are evaluated. RefractNet generally performed better when predicting $F$ as shown by average MSEs and FIDs. This difference likely arises from the logarithmic conversion from $F$ to $F_{dB}$ (Equation 3), which amplifies the influence of refractive structures present in the refractive domains, especially at longer ranges (Figure 5), during training. This suggests DNNs should be trained to estimate $F$, with subsequent calculation of desired gain or attenuation variables (e.g., $F_{dB}$, $P_L$) derived from the predicted $F$ values.

To explore this suggestion, RefractNet's predicted $F$ domain images from Experiment 1 (i.e., trained on $F$) are converted to $F_{dB}$ (Equation 3), and compared to TEMPER's $F_{dB}$ domain images using the evaluation metrics. These evaluation metrics are compared to Experiment 4 (Figure 7), which was trained on $F_{dB}$ and compared RefractNet's predicted $F_{dB}$ domain images to TEMPER's $F_{dB}$ images. Results show images of $F_{dB}$ converted from RefractNet-generated $F$ generally have more structural similarity to TEMPER's predicted $F_{dB}$ domain images than Experiment 4 but greater errors in estimated values (Figure 8).

Comparing the performance of all S-Band experiments, higher-altitude experiments consistently outperformed lower-altitude. This finding aligns with expectations, as higher-altitude scenarios contain more data points within the radar horizon and fully resolve patterns of constructive interference that occur over 30 m (Figure 9). Conversely, lower altitude scenarios contain more pixels outside of the radar horizon and don't fully resolve propagation structures occurring over 30 m (Figure 5). Therefore, future studies developing DNNs for radar applications aimed at identifying specific propagation features should carefully consider over what altitudes and ranges to evaluate and potentially even exclude data points within the radar horizon to enhance
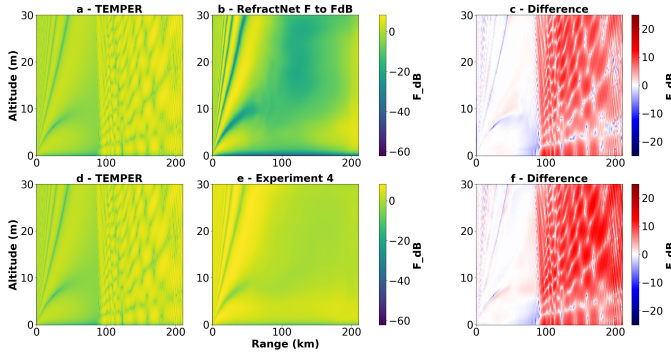
Figure 7: Refractive domain of $F_{dB}$ (a,d) from TEMPER, (b) calculated from Experiment 1 $F$ (c) the difference between a and b, (e) from Experiment 4, and (f) the difference between d and e.
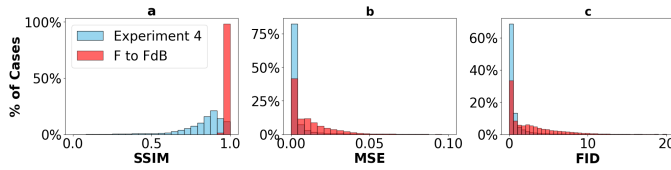


Figure 8: Distributions of (a) SSIM, (b) MSE, and (c) FID for Experiment 4 compared to the calculated $F_{dB}$ from Experiment 1 $F$.
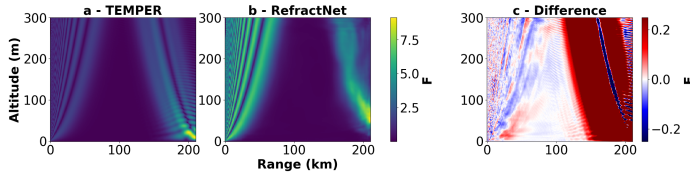


Figure 9: Refractive domain of $F$ calculated by (a) TEMPER, (b) RefractNet, and (c) the difference between these domains for a case from Experiment 7 where the evaluation metrics are: MSE = 0.004, FID = 0.83, and SSIM = 0.62.

model training and accuracy.

## Conclusion

This study introduced RefractNet, an image-to-image DNN generator designed for efficient simulation of the refractive environment, over both range and altitude, while accounting for multiple frequencies. RefractNet exhibited superior performance for X-band frequencies compared to S-band. From a practical standpoint, RefractNet demonstrated the capacity to handle both frequencies simultaneously. These results hold significant promise for the future of trained DNNs as a viable method to estimate the refractive environment, but also illustrate the sensitivity of predicting the refractive domain using DNNs. Results of this study varied considerably between training on different domain altitudes, $F$ or $F_{dB}$, single or multiple frequencies, and even training on $F$ and assessing performance using $F_{dB}$, thus, future work estimat-ing the refractive domain using DNNs need to carefully consider how training is approached.

## References

Bal, M.; Marey, A.; Ates, H. F.; Baykas, T.; and Gunturk, B. K. 2022. Regression of large-scale path loss parameters using deep neural networks. *IEEE Antennas and Wireless Propagation Letters* 21(8):1562–1566.

Barrios, A. E. 1994. A terrain parabolic equation model for propagation in the troposphere. *IEEE Transactions on Antennas and Propagation* 42(1):90–98.

Bean, B., and Dutton, E. 1968. Radio meteorology. national bureau of standards monogr.

Freehafer, J. E.; Fishback, W. T.; Furry, W. H.; and Kerr, D. E. 1951. Theory of propagation in a horizontally stratified atmosphere. IET.

Friis, H. T. 1946. A note on a simple transmission formula. *Proceedings of the IRE* 34(5):254–256.

Gündüz, D.; De Kerret, P.; Sidiropoulos, N. D.; Gesbert, D.; Murthy, C. R.; and Van der Schaar, M. 2019. Machine learning in the air. *IEEE Journal on Selected Areas in Communications* 37(10):2184–2199.

Isola, P.; Zhu, J.-Y.; Zhou, T.; and Efros, A. A. 2017. Image-to-image translation with conditional adversarial networks. In *Proceedings of the IEEE conference on computer vision and pattern recognition*, 1125–1134.

Lentini, N., and Hackett, E. 2015. Global sensitivity of parabolic equation radar wave propagation simulation to sea state and atmospheric refractivity structure. *Radio Science* 50(10):1027–1049.

Liao, Q.; Mai, Y.; Sheng, Z.; Wang, Y.; Ni, Q.; and Zhou, S. 2023. The comparison of long short-term memory neural network and deep forest for the evaporation duct height prediction. *IEEE Transactions on Antennas and Propagation* 71(5):4444–4450.

Moraitis, N.; Tsipi, L.; Vouyioukas, D.; Gkioni, A.; and Louvros, S. 2021. Performance evaluation of machine learning methods for path loss prediction in rural environment at 3.7 ghz. *Wireless Networks* 27(6):4169–4188.

Nguyen, C., and Cheema, A. A. 2021. A deep neural network-based multi-frequency path loss prediction model from 0.8 ghz to 70 ghz. *Sensors* 21(15):5100.

Pang, Y.; Lin, J.; Qin, T.; and Chen, Z. 2021. Image-to-image translation: Methods and applications. *IEEE Transactions on Multimedia* 24:3859–3881.

Pastore, D. M.; Wessinger, S. E.; Greenway, D. P.; Stanek, M. J.; Burkholder, R. J.; Haack, T.; Wang, Q.; and Hackett, E. E. 2022. Refractivity inversions from point-to-point x-band radar propagation measurements. *Radio Science* 57(2):1–16.

Popoola, S. I.; Jefia, A.; Atayero, A. A.; Kingsley, O.; Faruk, N.; Oseni, O. F.; and Abolade, R. O. 2019. Determination of neural network parameters for path loss prediction in very high frequency wireless channel. *IEEE access* 7:150462–150483.

Ronneberger, O.; Fischer, P.; and Brox, T. 2015. U-net: Convolutional networks for biomedical image segmentation. In *Medical image computing and computer-assisted intervention–MICCAI 2015: 18th international conference, Munich, Germany, October 5-9, 2015, proceedings, part III 18*, 234–241. Springer.

Rouseff, D. 1992. Simulated microwave propagation through tropospheric turbulence. *IEEE transactions on antennas and propagation* 40(9):1076–1083.

Ryan, F. J. 1991. User's guide for the vtrpe (variable terrain radio parabolic equation) computer model. *Final Report*.

Shu, B.; Zhang, W.; Chen, Y.; Sun, J.; and Wang, C.-X. 2023. Path loss prediction in evaporation ducts based on deep neural network. *IEEE Antennas and Wireless Propagation Letters*.

Tan, M., and Le, Q. 2019. Efficientnet: Rethinking model scaling for convolutional neural networks. In *International conference on machine learning*, 6105–6114. PMLR.

Torbunov, D.; Huang, Y.; Tseng, H.-H.; Yu, H.; Huang, J.; Yoo, S.; Lin, M.; Viren, B.; and Ren, Y. 2023a. Rethinking cyclegan: Improving quality of gans for unpaired image-to-image translation.

Torbunov, D.; Huang, Y.; Tseng, H.-H.; Yu, H.; Huang, J.; Yoo, S.; Lin, M.; Viren, B.; and Ren, Y. 2023b. Uvcgan v2: An improved cycle-consistent gan for unpaired image-to-image translation. *arXiv preprint arXiv:2303.16280*.

Wang, Z.; Bovik, A. C.; Sheikh, H. R.; and Simoncelli, E. P. 2004. Image quality assessment: from error visibility to structural similarity. *IEEE transactions on image processing* 13(4):600–612.

Wang, S.; Hu, S.-Y.; Cheah, E.; Wang, X.; Wang, J.; Chen, L.; Baikpour, M.; Ozturk, A.; Li, Q.; Chou, S.-H.; et al. 2020. U-net using stacked dilated convolutions for medical image segmentation. *arXiv preprint arXiv:2004.03466*.

Wang, H.; Cao, P.; Wang, J.; and Zaiane, O. R. 2022. Uctransnet: rethinking the skip connections in u-net from a channel-wise perspective with transformer. In *Proceedings of the AAAI conference on artificial intelligence*, volume 36, 2441–2449.

Wang, L.; Tang, J.; and Liao, Q. 2019. A study on radar target detection based on deep neural networks. *IEEE Sensors Letters* 3(3):1–4.

Xu, Z.; Cao, H.; Yin, Y.; Zhang, X.; Wu, L.; He, D.; and Wang, Y. 2021. Deep learning method for path loss prediction in mobile communication systems. In *2021 13th International Symposium on Antennas, Propagation and EM Theory (ISAPE)*, 01–03. IEEE.

Yang, Y.; Gao, F.; Ma, X.; and Zhang, S. 2019. Deep learning-based channel estimation for doubly selective fading channels. *IEEE Access* 7:36579–36589.

Yu, Y.; Zhang, W.; and Deng, Y. 2021. Frechet inception distance (fid) for evaluating gans. *China University of Mining Technology Beijing Graduate School* 3(11).

Zhang, Y.; Wen, J.; Yang, G.; He, Z.; and Wang, J. 2019. Path loss prediction based on machine learning: Principle, method, and data expansion. *Applied Sciences* 9(9):1908.

Zhu, J.-Y.; Park, T.; Isola, P.; and Efros, A. A. 2017. Unpaired image-to-image translation using cycle-consistent adversarial networks. In *Proceedings of the IEEE international conference on computer vision*, 2223–2232.

Zhu, X.; Li, J.; Zhu, M.; Jiang, Z.; and Li, Y. 2018. An evaporation duct height prediction method based on deep learning. *IEEE Geoscience and Remote Sensing Letters* 15(9):1307–1311.